# TRANSIENT CONVECTION FROM FORCED TO NATURAL WITH FLOW REVERSAL FOR CFD VALIDATION

**Blake W. Lance and Barton L. Smith**
Utah State University
Mechanical & Aerospace Engineering
4130 Old Main Hill, Logan Utah, USA
b.lance@aggiemail.usu.edu, barton.smith@usu.edu

### ABSTRACT

Transient convection was investigated experimentally for the purpose of providing Computational Fluid Dynamics (CFD) validation data. A specialized facility for validation experiments called the Rotatable Buoyancy Tunnel was used to acquire thermal and velocity measurements of flow over a smooth, vertical heated wall. The initial condition was forced convection downward with subsequent transition to mixed convection, ending with natural convection upward after a flow reversal. Data acquisition through the transient was repeated for ensemble-averaged results. The flow transient was similar to a Loss of Forced Convection in the Gen. IV Very High Temperature Reactor (VHTR). Although models have shown that the transient of peak clad temperature takes hours to days, the flow conditions during the short time of the flow reversal determine the subsequent long-term conditions. This transient and buoyancy-driven flow is challenging for CFD, but is critical in the safety analysis of the VHTR. With simple flow geometry, validation data were acquired at the benchmark level. All boundary conditions (BCs) were measured and their uncertainties quantified. Temperature profiles on all four walls and the inlet were measured, as well as as-built test section geometry. Inlet velocity profiles and turbulence levels were quantified using Particle Image Velocimetry. System Response Quantities (SRQs) were measured for comparison with CFD outputs and include velocity profiles, wall heat flux, and wall shear stress. Results from an Unsteady Reynolds-Averaged Navier-Stokes model are also presented and compared with experimental results. Extra effort was invested in documenting and preserving the validation data. Details about the experimental facility, instrumentation, experimental procedure, materials, BCs, and SRQs are made available through this paper with the latter two available for download. To ensure longevity, the data and associated details will be published in journal format with links to tabulated data.

## 1 INTRODUCTION

### 1.1 The Very High Temperature Reactor

The VHTR concept is the most prominent of the possible Next Generation Nuclear Plant designs under consideration [1]. There are several advantages to this design over currently-operating plants including improved efficiency from increased temperatures between 900-950°C, more passive safety features, potential for process heat or hydrogen production at co-located plants, and an increase from a 40 to 60 year license cycle. The VHTR uses helium gas as the coolant so high temperatures can be realized and efficiency can thus be increased. The core design is either a prismatic core where most of the reactor core is graphite with coolant and fuel passages or a pebble bed core with fuel elements the size of tennis balls. In either design, normal operation has helium forced downward through the core [1, 2]. In the event of Loss of Forced Convection (LOFC), viscous and buoyancy forces initially decrease flow rate and eventually buoyancy forces reverse the flow to steady natural convection. Natural convection is the primary mode of heat removal from the core in a Pressured Conduction Cooldown event. This phenomenon has been identified to be one of high importance and low knowledge by the U.S. Nuclear Regulatory Commission (NRC) [3].

### 1.2 Computational Fluid Dynamics Validation

In the safety analysis required for new reactor designs, the NRC and Department of Energy use system codes such as RELAP5, TRACE, and MELCOR to model coupled physics for transient accident scenarios such as the LOFC. These codes have been heavily validated against experimental data. RELAP5 has traditionally been one dimensional in space, but recently efforts are moving towards three dimensional codes to resolve complex flows in and near the reactor core. With this shift toward CFD and CFD-like codes, more comprehensive validation data are required.

To understand the need for experiments expressly aimed at providing validation data, one must first understand the different aims of validation and discovery experiments. Generally older experimental data from discovery experiments are not sufficiently described to be used for validation. Discovery experiments are common in research where new physical phenomena are measured, presented, and discussed. Validation experiments do not necessarily measure unique phenomena but the measurement process and description are more complete [4].

The motivation for performing a validation experiment is to provide the information required to quantify the uncertainty of a mathematical model. This uncertainty helps decision makers and managers to quantify the credibility of the model. The ASME V&V 20 Standard [5] outlines an approach to estimate the validation comparison error and the validation uncertainty. The validation error $E$ is the difference between the simulation result $S$ and the validation experiment result $D$ as

$$E = S - D. \tag{1}$$

The validation uncertainty gives perspective to the error by considering both numerical and experimental uncertainty and is calculated as

$$u_{val} = \sqrt{u_{num}^2 + u_{input}^2 + u_D^2} \tag{2}$$

where $u_{num}$ is the numerical uncertainty, $u_{input}$ is the model input uncertainty, and $u_D$ is the experimental data uncertainty. The numerical uncertainty is estimated from solution verification with sources such as iterative and discretization uncertainty. The latter two uncertainties accompany validation data. The uncertainty in the measured boundary conditions (BCs) that are used for model inputs is $u_{input}$. The uncertainty of system response quantities (SRQs)—data used to compare system outputs—is $u_D$. If $|E| >> u_{val}$, one can conclude model error remains. But if $|E| \leq u_{val}$ and $u_{val}$ is acceptably small for the intended use of the model, the validation error may be satisfactory. These general equations show that validation data and their uncertainty are necessary to assess model accuracy via model validation.

There are several tiers of detail in validation experiments. The Benchmark Tier, also called Separate Effects Testing, requires that all model inputs and most model outputs are measured and experimental uncertainty is included [6]. To meet the requirements of this tier in the validation hierarchy, the hardware used in this study is specially fabricated to validate specific aspects of flow over a heated wall. The heated wall represents a reactor component convecting heat to the coolant.

## 1.3 Transient Flows

Some studies of non-periodic transient flow have been performed, but as He & Jackson note, only recently has technology allowed for comprehensive measurements of ensemble averaged transient experiments [7]. This review covers adiabatic and convective ramp-type flow transients. Most of the first experiments measured either temperature of tube walls or velocity, but not both. A common observation was that accelerating flow suppresses turbulence while decelerating flow augments it.

The first work by Koshkin *et al.* was published in 1970 for turbulent air flow. This study reported measurements during a change in electrical power and different flow transients, measuring and reporting temperature [8]. Two similar studies were published in the 1970s and used electrochemical techniques with probes to measure velocity profiles inside a tube from a step change in flow rate [9, 10].

Rouai [11] performed heat transfer experiments on ramp-up and ramp-down transients as well as periodic pulsating flow with a non-zero time mean. Water was heated by passing an alternating electrical current through a stainless steel tube. Temperature measurements were made by 24 thermocouples (TCs) welded to this tube. Flow transients were prescribed by using a constant head tank and varying the flow through the test section by a valve. Wall heat flux remained constant and changes in wall temperature were measured. The observed Nusselt number departed more from the psuedo-steady values for faster transients and for decelerating flows, likely from the augmentation of turbulence.

Jackson *et al.* performed a study on non-periodic ramping transients in a water tube [12]. It was similar to that by Rouai but measured local fluid temperature with a TC probe and improved computer control and data logging for greater repeatability and ensemble averaging. The TC probe was small enough to capture turbulent fluctuations. They also found a suppression of turbulence and consequently wall heat transfer for accelerating ramps and augmentation during decelerating ramps. They also observed a peak in temperature fluctuations soon after the start of the ramps.

He & Jackson performed experiments in water using two-component LDA measurements in a clear, unheated tube. This non-intrusive velocity measurement was one of the first known to the authors for non-periodic flows. Ensemble averaged results were used for mean and turbulent quantities. The turbulent results were shown to deviate from psuedo-steady results for short transients. Several nondimensional parameters were recommended for ramp-type transients [7].

Barker and Williams [13] reported high speed measurements of an unsteady flow with heat transfer in air. They used a hot wire anemometer, a cold wire temperature probe, and a surface heat flux sensor to measure heat transfer coefficients for fully-developed turbulent pipe flow. Most results were for periodic flows, but some were presented for ramp-type transients with negligible buoyancy effects. The measurements were basic and provided data for conceptual model development.

In the previous studies, little coupling of velocity and thermal measurements was found for flow transients and buoyancy effects were negligible. Also, as these were discovery experiments, boundary conditions were not measured and provided as tabulated data, making the results of limited use for validation. The facility description is very basic and flow geometries simplified. The current study contributes high fidelity measurements of a ramp-down transient suitable for validation studies with simultaneous, non-intrusive velocity and thermal measurements to provide validation data on simplified geometry for three-dimensional LOFC-type simulations.

## 2 EXPERIMENTAL FACILITY

The Rotatable Buoyancy Tunnel (RoBuT) was designed specifically for CFD validation experiments. The wind tunnel was built onto a rotational frame (like a ferris-wheel) to enable both buoyancy-aided and buoyancy-opposed forced/mixed convection, as well as natural convection using the same inlet in all cases. A photo of the RuBuT showing the overall layout is shown in Fig. 1a and a sketch of the important flow components is shown in Fig. 1b. The contraction contained a flow straightener and screens. The blower drew air through the test section from top to bottom. The cameras and laser were part of the Particle Image Velocimetry (PIV) system shown in the two non-mapped, two-component configuration for SRQ data as described below. The coordinate system had $x$ in the streamwise direction, $y$ normal to the wall, and $z$ in the spanwise direction. The origin was at the spanwise center of the leading edge on the heated wall as shown.

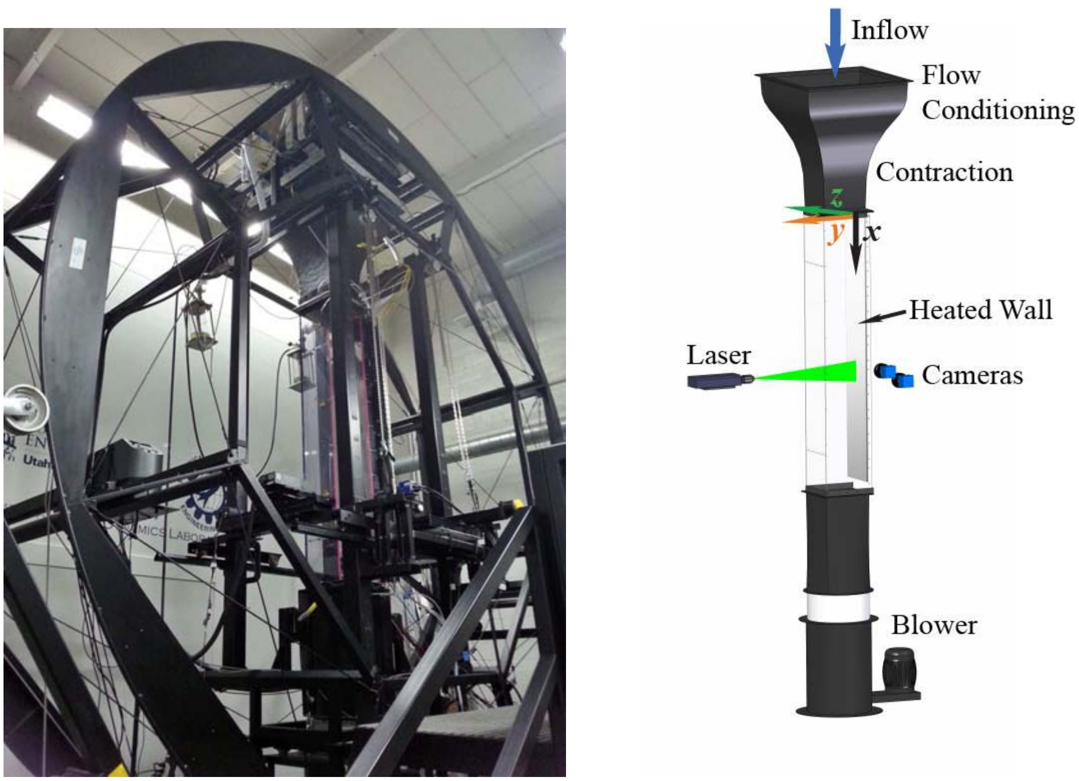


**(a) RoBuT photo** **(b) RoBuT sketch**

**Figure 1. The experimental facility in the buoyancy opposed orientation**

### 2.1 Test Section

The test section was 0.305 m × 0.305 m in cross section and two meters long. Three walls were made of clear Lexan® for optical access that were 12.7 mm thick. The fourth wall was a composite with layers of aluminum, polyimide, thermal epoxy, silicon heaters, and thermal insulation as shown in Fig. 2. The surface plate was 3.18-mm thick aluminum that was nickel coated to about 0.05 mm to suppress thermal radiation. The resulting normal emissivity was both predicted and measured to about 0.03 [14]. Next was 1.02 mm of thermal epoxy and 0.254 mm of Kapton®. The Heat Flux Sensors were placed into rectangular holes in the

Kapton® to generate nearly uniform thermal resistance. A 6.35-mm aluminum plate provided rigidity for the inside section and aided in uniform heat distribution from the heaters to the surface plate. The heaters were 1.59-mm thick silicone rubber. The thermal insulation was 25.4 mm thick. A 6.35-mm aluminum back plate provided additional strength. The edges of this layered plate were thermally insulated by 12.7-mm thick Teflon® to reduce side wall heating. This design allowed for heating as well as temperature and heat flux measurements within the wall.

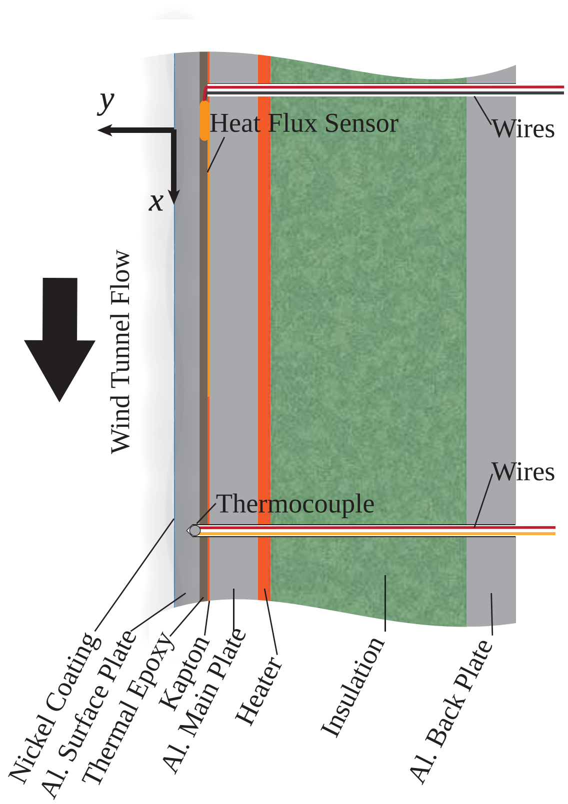


**Figure 2. Heated Wall cross section**

A total of 312 TCs were used with 15 suspended in the inlet flow conditioning to measure air temperature, 63 in the three clear walls, and the remainder within the heated wall. The embedded TCs were within 3.18 mm of the measured surface and potted with thermal epoxy. These provided thermal boundary conditions. Three RDF Corp. model 20457-3 thin-film heat flux sensors were potted inside the heated wall, about 4 mm below the surface, for SRQ measurements. Both types of thermal instrumentation were measured with 21 National Instruments NI-9213 TC modules in five NI-cDAQ-9188 chassis. The TCs were calibrated with these modules and have a total uncertainty of 1°C. More details on the design and construction of the heated wall are found in [14].

## 2.2 PIV System

Air velocity fields were acquired using PIV. This technique has several relevant advantages including full-field, unobtrusive measurements for rapid data acquisition. The inflow was measured in five planes spaced in $z$ with two-component (one camera) PIV. The SRQ velocity at the spanwise center, wall normal plane were acquired with two simultaneous, two-component measurements. These two measurements allowed flow fields to be interrogated at two resolutions in the same laser sheet, one across the entire 30.5-cm test section span and the other at the 3.5-cm span nearest the heated wall. The wide field of view captured the bulk flow with vector spacing of ~9.13 mm while the narrow field of view resolved near-wall velocity for shear measurements with vector spacing of ~0.97 mm.

The cameras were model Imager sCMOS from LaVision Inc. with a $2560 \times 2160$ pixel sensor. A Nikon Nikkor 28-mm lens was used on both the inflow measurements and the wide field-of-view camera for SRQ data. A Nikkor 105-mm lens, with two extension tubes totaling 39.5 mm, were used for the narrow field-of-view for SRQ data. DaVis 8.2 software was used to acquire and process the particle images. Since the bulk velocity changed through the transient, the time between image acquisitions ($dt$) was changed so maximum particle displacements were 8-32 pixels. Interrogation windows were round gaussian weighted to reduce correlation noise. The initial region size was $128 \times 128$ pixels and was reduced to $32 \times 32$ pixels with 75% overlap. Initial and intermediate region sizes used two passes and the final size used four passes. The laser was a dual cavity frequency doubled Nd:Yag model with about 22 mJ/pulse at 532 nm. Olive oil tracer particles were produced in a Laskin Nozzle [15]. These particles were measured to have a mean diameter around 1 µm using a TSI Aerodynamic Particle Sizer Spectrometer at the RoBuT outlet in the measurement configuration.

## 3 EXPERIMENTAL CONDITIONS

For improved statistics, the data were ensemble averaged over repeated runs. A total of 2400 runs were used, with 100-200 for each PIV acquisition location and $dt$. Steady thermal conditions triggered data acquisitions and simultaneously cut power to the blower, initiating transient conditions. Heater power was fixed through each run.

LabView was used to control the conditions and to acquire thermal data via a National Instruments data acquisition system. This system created the master TTL clock and also triggered the PIV system for synchronized thermal and velocity data acquisition. Data were acquired at 5 Hz for a period of 20.2 s. The initial condition was forced convection downward as in the VHTR with the heated wall at 130°C. Blower power was removed and the drum-type blower was allowed to coast to a stop over about 10 s. This resulted in ramp-down bulk velocity and subsequent flow reversal by natural convection. The bulk velocity at the test section inlet at the centerline plane is shown in Fig. 3. The bulk velocity approaches zero at the end since there is both natural convection upward near the heated wall and recirculating flow downward far from the wall. There was measurable delay in the blower drive system, so $t = 0$ was prescribed as the last phase where the bulk velocity matched the initial condition. Thus, the useful transient time spans $0 \leq t \leq 18.2$ s and data are presented in this range.

Table I shows the streamwise locations $x$ where PIV and heat flux data were acquired at the spanwise center with the associated $\mathrm{Re}_x$ at the initial condition and $\mathrm{Gr}_x$ where $\mathrm{Re}_x = U_\infty x/\nu$ and $\mathrm{Gr}_x = g\beta(T_s - T_\infty)x^3/\nu^2$. The free-stream velocity is $U_\infty$, $\nu$ is the kinematic viscosity, $g$ is the acceleration due to gravity, $\beta$ is the fluid thermal coefficient of expansion, $T_s = 130°\mathrm{C}$ and $T_\infty = 20°\mathrm{C}$ are the temperatures of the surface and fluid respectively. External coordinates were used as the boundary layers generally do not meet as in fully-developed pipe flow. Fluid properties were evaluated at the film temperature.

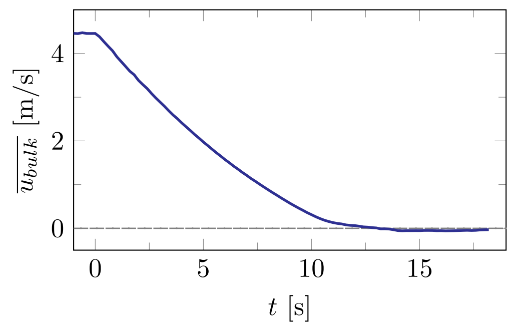


**Figure 3. Bulk velocity across the inlet at the spanwise center ($z$ = 0) through time**

**Table I. $\mathrm{Re}_x$ at the initial condition and $\mathrm{Gr}_x$ at the three locations in $x$ at the spanwise center where SRQ data were acquired**

| | $x$ [m] | $\mathrm{Re}_x(t{=}0)$ | $\mathrm{Gr}_x$ |
|---|---|---|---|
| $x_1$ | 0.16 | 36,000 | $3.10 \times 10^7$ |
| $x_2$ | 0.78 | 175,000 | $3.45 \times 10^9$ |
| $x_3$ | 1.39 | 310,000 | $1.98 \times 10^{10}$ |

## 4 RESULTS

Because the purpose of this work is to provide validation data, BCs and SRQs are the main results. The boundary conditions included as-built geometry measurements of the inside of the test section, temperatures on the inflow and four walls, ensemble averaged and fluctuating velocity profiles at the inlet, and the atmospheric conditions for fluid properties at room temperature. The SRQs included ensemble averaged and fluctuating velocity profiles across the test section, heat flux at the heated wall, and shear on the heated wall. These quantities are summarized in Table II. The results were for locations within the domain at three streamwise locations in $x$ at the spanwise center as specified in Table I.

**Table II. The available experimental data presented in this work separated into BC and SRQ types**

| BCs | SRQs |
|---|---|
| As-Built Geometry | Velocity Profiles |
| Wall Temperatures | Reynolds Stress Profiles |
| Inlet Temperature | Wall Heat Flux |
| Inlet Velocity | Wall Shear |
| Atmospheric Conditions | |

### 4.1 Boundary Conditions

The boundary conditions are organized in comma separated files formatted for upload into Star-CCM+, though the format can be easily adapted for use in other CFD software. Included are the coordinates $x, y, z$ in meters with the ensemble average values, bias uncertainty (B), precision uncertainty (P), and total uncertainty (U) of each quantity of interest. The Inlet-uvw.csv file contains ensemble averaged velocities, specific Reynolds stresses, and their uncertainties at the inlet at the five measurement profiles that span $y$. The Reynolds stresses have unique positive and negative uncertainties. For example, uncertainties of $\overline{u'u'}$ are specified as Uuup and Uuum. The data units and time-stamps are specified in column headers. Also included in the files are the as-built geometry measurements and a parasolid file generated from these measurements. All uncertainties are at the 95% confidence level. They can be downloaded at https://dl.dropboxusercontent.com/u/14316438/TransientBCs.zip.

### 4.2 CFD Simulation

The purpose of the CFD exercise was to ensure the data acquired were sufficient for validation. Simulations were performed using Star-CCM+ 9.06 [16] using the experimental boundary conditions. The implicit unsteady model was used in combination with the Low-Re $\overline{v^2} - f$, $k - \epsilon$ Reynolds-Averaged Navier-Stokes (RANS) model [17]. This model has been found to perform well with buoyant flows in vertical channels [18]. Air was modeled as an ideal gas with properties as functions of temperature. Thus, buoyancy is modeled directly. Coupled momentum and coupled energy were also used to capture natural convection. Solvers were second-order accurate in space and time. As-built geometry was used for the fluid domain. An example of the measured BCs being used in the simulation is shown in Fig. 4 and shows temperatures mapped onto the fluid domain.

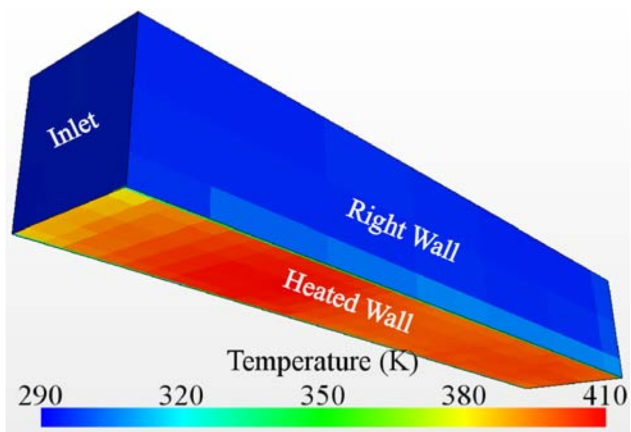


**Figure 4. Experimental temperatures at the initial condition mapped onto the test section. The development of the thermal boundary layer is seen on the Right Wall as the air moves from the Inlet through the domain.**

All normalized residuals were driven to below $1 \times 10^{-6}$ at every time step. The time step was chosen for a particle to displace about one cell length in the streamwise direction. Converged solutions were obtained for three meshes of 15.625k, 125k, and 1M cells with equivalent cell counts in each direction of 25, 50, and 100, respectively. Cells were concentrated near the walls. The configuration of the cross section for the finest mesh is shown in Fig. 5. The cell size in each direction and the time step were reduced by a factor of two with each refinement. The maximum wall $y^+$ values were 1.5, 0.76, and 0.36, respectively. Three meshes allowed for the Grid Convergence Index method first proposed by Roache and improved upon by others [6, 19]. The safety factor was allowed to increase to compensate for results with less consistency. These results are at the 95% confidence level and are used as uncertainty bands for CFD outputs in Figs. 6 and 8.

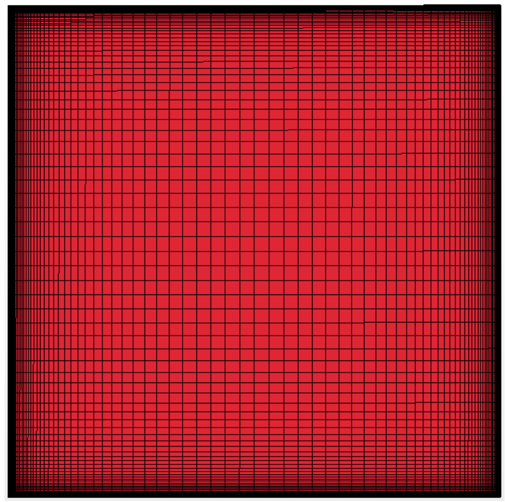

**Figure 5. The cross-section of the structured rectangular mesh with 1M cells**

### 4.3 System Response Quantities

The SRQs were the experimental results within the test section domain at the three streamwise ($x$) locations. They include ensemble average velocity, specific Reynolds stresses, wall heat flux, and wall shear stress.

Profiles of streamwise velocity $u$ and turbulent kinetic energy $k$ are shown in Fig. 6 at three locations in $x$ for the top ($x_1$), middle ($x_2$), and bottom ($x_3$). The definition $k = \frac{1}{2}\left(\overline{u'u'} + \overline{v'v'} + \overline{w'w'}\right)$ was used, assuming $\overline{w'w'} = \overline{v'v'}$ since the third component of velocity was not measured. The specific Reynolds stresses $\overline{u'u'}$ and $\overline{v'v'}$, as well as $\overline{u'v'}$, were directly measured and provided with SRQ data. Since the CFD model was a modified two-equation RANS, the Reynolds stresses are not available and $k$ was the logical choice for an SRQ.

The uncertainty bands on CFD data are from the grid convergence study described in Sec. 4.2. PIV uncertainties are from the Uncertainty Surface Method and consider bias uncertainty from particle displacement, particle image density, particle image size, and shear originally described in [20] and improved upon with methods from [21]. Precision uncertainty was calculated by methods of Wilson & Smith [22]. Total uncertainty was calculated by the root-sum-square of the bias and precision uncertainties at the 95% confidence level.

The streamwise velocity $u$ profiles from PIV and CFD show acceptable consistency through the transient. The boundary layer thickness increases in the streamwise direction $x$ at the initial condition as expected. There is a small difference in the bulk velocity in PIV and CFD results at this initial condition, perhaps due to a discrepancy in the inflow velocity mapping in the direction not measured. Any errors here are not inherent in the provided BCs as inflow mapping is left to the modeler. The velocity profile shape generally remains similar but is reduced in magnitude during the first four seconds. At $t = 8$ s, the contribution from natural convection begins affecting the profiles near the heated wall ($y = 0$). At $t = 12$ s the profiles show a strong influence from natural convection. The large uncertainty bands for $x_3$ and large $y$ are from the flow reversal phenomena not being mesh converged locally in the CFD. The changes from $t = 12 - 16$ s is subtle as steady natural convection is reached. The uncertainty bands are generally small on both PIV and CFD results and do not overlap, suggesting remaining model uncertainty which is not represented nor easily quantified.

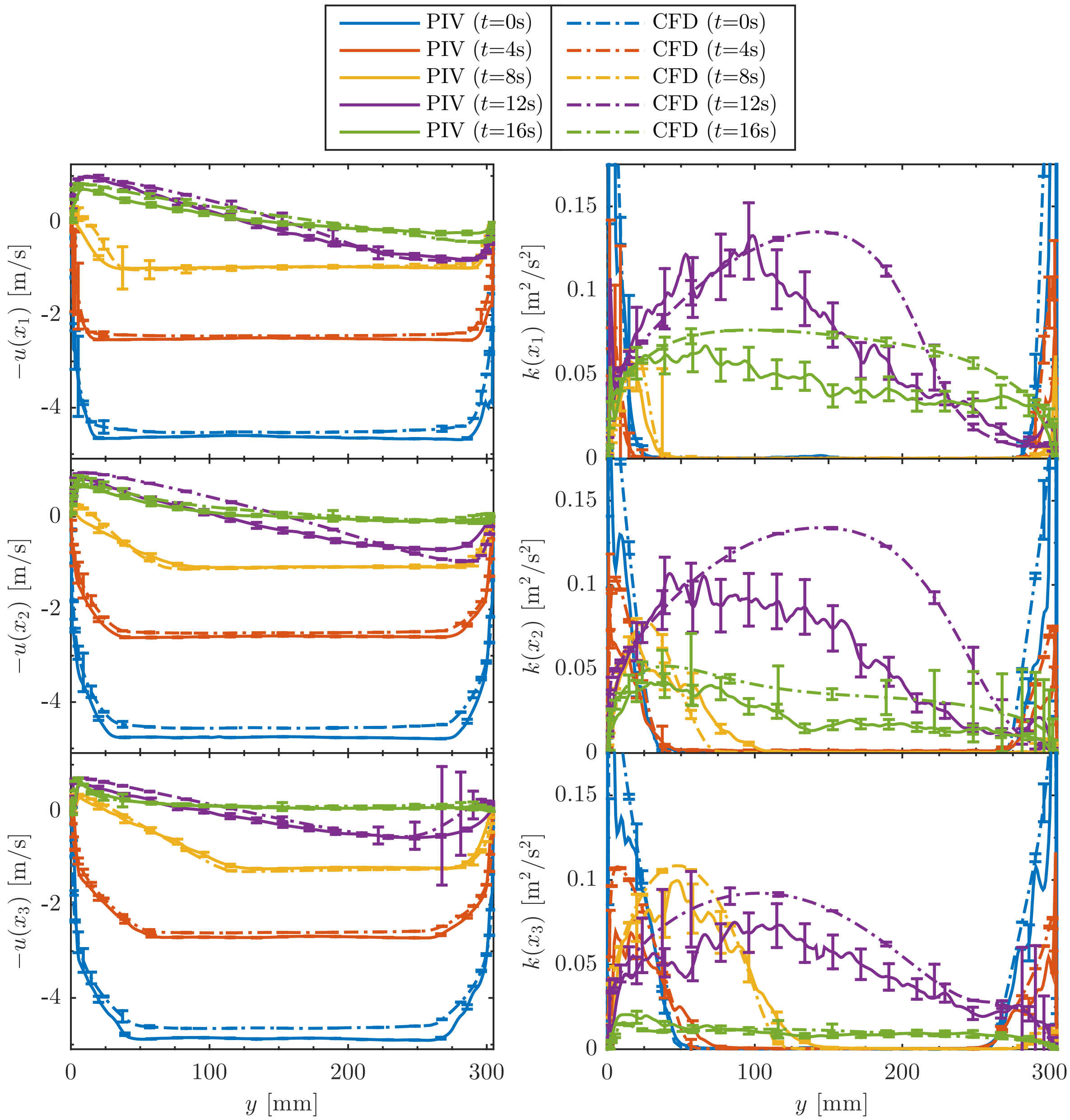


**Figure 6. The streamwise velocity *u* and turbulent kinetic energy *k* for both PIV and CFD results**

The results for turbulent kinetic energy $k$ are similar but have greater spatial variability and uncertainty. Initially $k$ is elevated near both walls as expected. The influence of natural convection increases $k$ near the heated wall initially. The area of elevated $k$ moves away from the wall over time. The phase of $t = 12$ s has the highest levels, likely from a chaotic flow reversal. The final measured state has reduced kinetic energy and may still be decreasing. Again, the uncertainty bands generally do not overlap suggesting remaining model uncertainty.

Previous methods to quantify wall shear have fit experimental velocity data with empirical correlations such as Spalding or Musker profiles with high accuracy [23]. This method works well for steady boundary layer data where the profiles are an accurate representation of velocity, but not for the transient conditions in the current study. Therefore wall shear stress was calculated directly from PIV data as $\tau_s = \mu \frac{\partial u}{\partial y}\big|_{y=0}$ where $\tau_s$ is wall shear stress and $\mu$ is dynamic viscosity. High-resolution PIV data were used to fit a line to velocity data where $y^+ = yu_\tau/\nu \leq 5$ for $\frac{\partial u}{\partial y}\big|_{y=0}$, where $u_\tau = \sqrt{\tau_s/\rho}$ and $\rho$ is the fluid density [24]. Initially 10 points were included in the fit and a stable iterative method was used to calculate $\tau_s$ and the number of data points to fit within $y^+ \leq 5$. The wall was located by the particle images with a mask carefully defined. The linear fit was performed using linear regression with more weight given to velocity data with lower uncertainty [25]. The high-resolution PIV data at $x_2$ and associated linear fit are shown in Fig. 7 for five phases of the transient. The fit was not forced to the wall as wall location errors would be compounded and not easily quantifiable in the uncertainty. The dynamic viscosity was evaluated using Sutherland's Law at the wall temperature. The fit uncertainty was combined with the viscosity uncertainty using the Taylor Series Method [26].

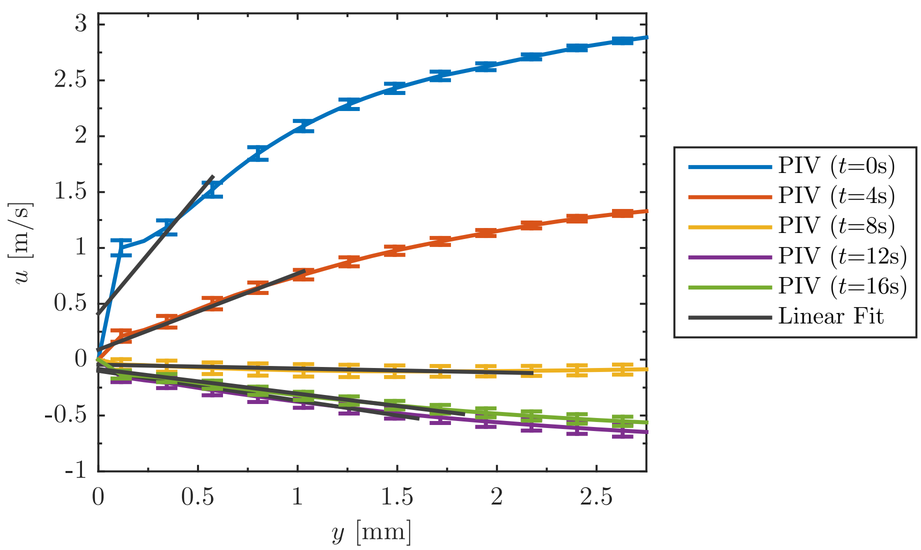


**Figure 7. High-resolution PIV data near the heated wall with linear fit**

Results for the scalars of wall heat flux and wall shear stress are shown in Fig. 8 at the same three $x$ locations through time with their associated uncertainty bands. The experimental heat flux came from the Heat Flux Sensors (HFSs) using the manufacturer-calibrated sensitivity. The uncertainty included 5% bias while the precision values were measured.

The heat flux results of the experiment and CFD are not in good agreement as shown in Fig. 8. The experimental results from the HFSs show a low sensitivity to convection due to the thermal capacitance of the heated wall, but the CFD had no capacitance modeled. Also, the CFD mesh was not well refined when considering heat flux as noted by large uncertainty bands. Further efforts should be made in CFD to model capacitance and refine the mesh.

The wall shear results have better agreement between PIV and CFD results. The experimental measurements are somewhat noisy at high levels of shear, likely from the decreased accuracy of PIV data near walls. When the shear decreases, more points can be used in the fit for smoother results. The uncertainty bands on the CFD results suggest that the mesh may not be well resolved in regions of flow reversal near the heated wall.

Like the BC data, the SRQ data and their uncertainties are tabulated for use in validation studies. They are contained in comma separated files with the *.csv extension and can be opened in a spreadsheet program or a simple text editor. All resulting PIV data are made available from both cameras (Cam1 is high resolution and Cam2 is large field of view) with headers similar to the BC PIV data presented earlier. They contain

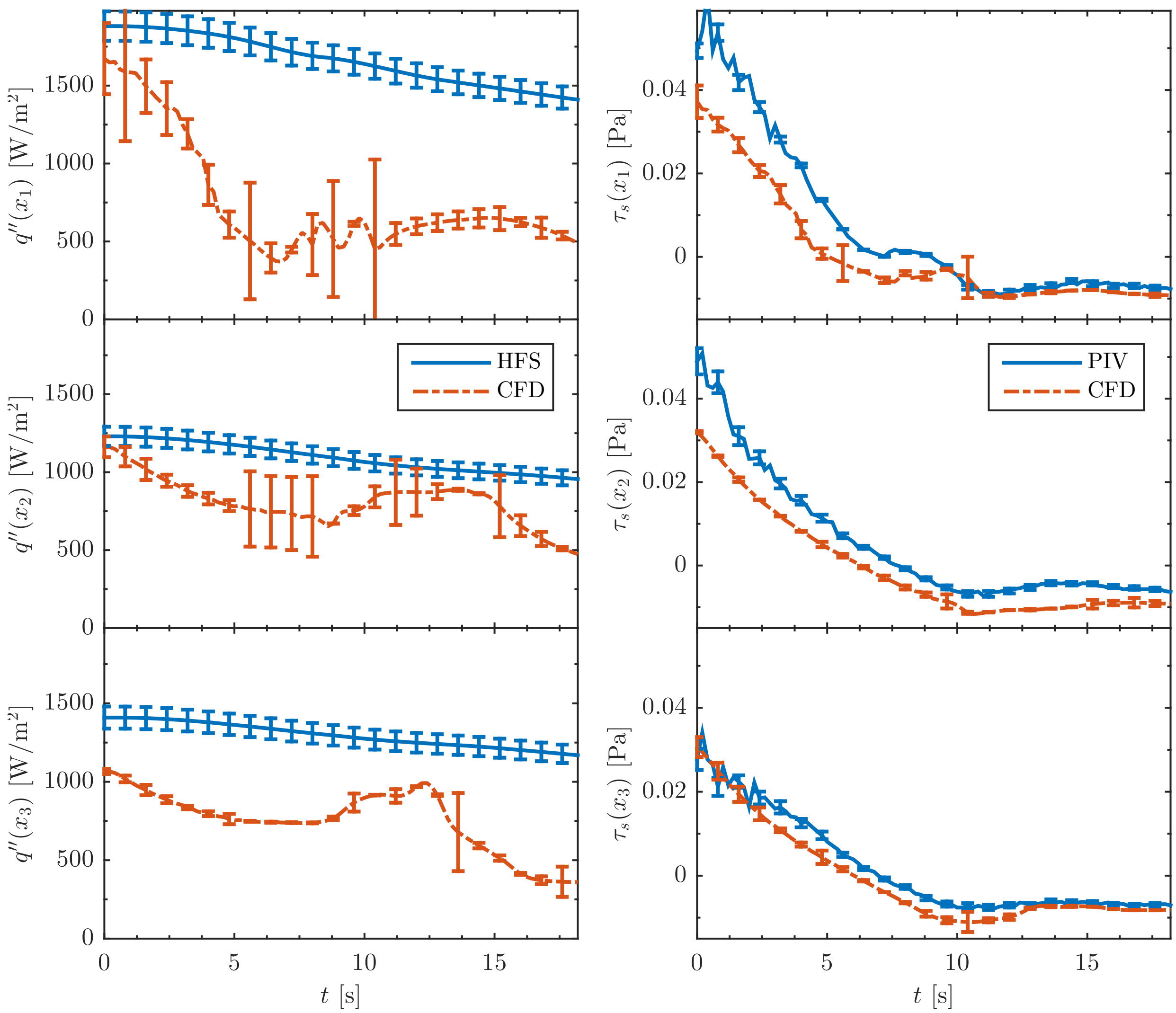


**Figure 8. The heated wall heat flux and wall shear stress plotted over time for both PIV and CFD results**

data at all three $x$ locations as specified in the files. As with the BC data, the full uncertainties at 95% confidence are provided with unique positive and negative uncertainties for Reynolds stresses. Wall heat flux results are given for all three sensors along $x$ with specified bias, precision, and total uncertainty. Wall shear is similarly formatted and has the total uncertainty. These data are compressed and can be downloaded at https://dl.dropboxusercontent.com/u/14316438/TransientSRQs.zip.

## 5 CONCLUSIONS

This paper presents the study of a ramp-down flow transient with heat transfer and buoyancy effects in simplified geometry to provide CFD validation data. Repeated runs provide high resolution data for ensemble averaging and turbulent statistics of high resolution data. The provided BCs and SRQs, listed in Table II for the conditions in Table I, are tabulated and available for download. Uncertainty is also included for all presented data. The data contain rich and comprehensive coverage of this flow. They enable validation studies to assess model accuracy and are necessary to calculate simulation uncertainty.

## ACKNOWLEDGMENTS

This research was performed using funding received from the DOE Office of Nuclear Energy's Nuclear Energy University Programs, and their support is gratefully acknowledged. Also, the authors appreciate Dr. Nam Dinh who originally suggested transient convection for CFD validation.

## REFERENCES

[1] U. S. Department of Energy, "Next Generation Nuclear Plant: A Report to Congress," Technical report, U. S. Department of Energy Office of Nuclear Energy (2010).

[2] C. Oh, E. Kim, R. Schultz, M. Patterson, D. Petti, and H. Kang, "Comprehensive Thermal Hydraulics Research of the Very High Temperature Gas Cooled Reactor," *Nuclear Engineering and Design*, **240**(10), pp. 3361–3371 (2010), doi:10.1016/j.nucengdes.2010.07.007.

[3] B. G. Woods, R. B. Jackson, and B. L. Nelson, "Scaling Analysis for the Very High Temperature Reactor Test Facility at Oregon State University," Technical report, Oregon State University (2009).

[4] P. J. Roache, *Fundamentals of Verification and Validation*, Hermosa Publ. (2009).

[5] ASME, "ASME V&V 20-2009: Standard for Verification and Validation in Computational Fluid Dynamics and Heat Transfer," Standard, American Society of Mechanical Engineers (2009).

[6] W. L. Oberkampf and C. J. Roy, *Verification and Validation in Scientific Computing*, Cambridge University Press (2010).

[7] S. He and J. D. Jackson, "A Study of Turbulence Under Conditions of Transient Flow in a Pipe," *Journal of Fluid Mechanics*, **408**, pp. 1–38 (2000), doi:10.1017/s0022112099007016.

[8] V. Koshkin, E. Kalinin, G. Dreitser, B. Galitseisky, and V. Izosimov, "Experimental Study of Nonsteady Convective Heat Transfer in Tubes," *International Journal of Heat and Mass Transfer*, **13**(8), pp. 1271–1281 (1970), doi:10.1016/0017-9310(70)90068-2.

[9] K. Kataoka, T. Kawabata, and K. Miki, "The Start-up Response of Pipe Flow to a Step Change in Flow Rate," *Journal of Chemical Engineering of Japan*, **8**(4), pp. 266–271 (1975), doi:10.1252/jcej.8.266.

[10] T. Maruyama, T. Kuribayashi, and T. Mizushina, "The Structure of the Turbulence in Transient Pipe Flows," *Journal of Chemical Engineering of Japan*, **9**(6), pp. 431–439 (1976), doi:10.1252/jcej.9.431.

[11] N. M. Rouai, *Influence of Buoyancy and Flow Transients on Turbulent Convective Heat Transfer in a Tube*, Ph.D. thesis, University of Manchester, UK (1987).

[12] J. D. Jackson, O. Büyükalaca, and S. He, "Heat Transfer in a Pipe Under Conditions of Transient Turbulent Flow," *International Journal of Heat and Fluid Flow*, **20**(2), pp. 115–127 (1999), doi:10.1016/s0142-727x(98)10056-5.

[13] A. R. Barker and J. E. F. Williams, "Transient Measurements of the Heat Transfer Coefficient in Unsteady, Turbulent Pipe Flow," *International Journal of Heat and Mass Transfer*, **43**(17), pp. 3197–3207 (2000), doi:10.1016/s0017-9310(99)00305-1.

[14] J. R. Harris, B. W. Lance, R. E. Spall, and B. L. Smith, "Transient Mixed Convection Validation Facility and Study," 15-356, The 15th International Topical Meeting on Nuclear Reactor Thermal Hydraulics (NURETH), Pisa, Italy (May 12-16, 2013).

[15] C. J. Kähler, B. Sammler, and J. Kompenhans, "Generation and Control of Tracer Particles for Optical Flow Investigations in Air," *Experiments in Fluids*, **33**, pp. 736–742 (2002), doi:10.1007/s00348-002-0492-x.

[16] CD-Adapco, *Star-CCM+ User Guide*, 9.06 edition.

[17] L. Davidson, P. Nielsen, and A. Sveningsson, "Modifications of the $\overline{v^2} - f$ Model for Computing the Flow in a 3D Wall Jet," Proceedings of the International Symposium on Turbulence, Antalya, Turkey (October 12-17, 2003).

[18] L. E. Moutaouakil, Z. Zrikem, and A. Abdelbaki, "Performance of Various RANS Eddy-viscosity Models for Turbulent Natural Convection in Tall Vertical Cavities," *Heat Mass Transfer*, **50**(8), pp. 1103–1113 (2014), doi:10.1007/s00231-014-1322-4.

[19] P. J. Roache, "Quantification of Uncertainty in Computational Fluid Dynamics," *Annual Review of Fluid Mechanics*, **29**(1), pp. 123–160 (1997), doi:10.1146/annurev.fluid.29.1.123.

[20] B. H. Timmins, B. W. Wilson, B. L. Smith, and P. P. Vlachos, "A Method for Automatic Estimation of Instantaneous Local Uncertainty in Particle Image Velocimetry Measurements," *Experiments in Fluids*, **53**(4), pp. 1133–1147 (2012), doi:10.1007/s00348-012-1341-1.

[21] S. O. Warner and B. L. Smith, "Autocorrelation-based Estimate of Particle Image Density for Diffraction Limited Particle Images," *Measurement Science and Technology*, **25**(6), p. 065201 (2014), doi:10.1088/0957-0233/25/6/065201.

[22] B. M. Wilson and B. L. Smith, "Taylor-series and Monte-Carlo-method Uncertainty Estimation of the Width of a Probability Distribution Based on Varying Bias and Random Error," *Meas. Sci. Technol.*, **24**(3), p. 035301 (2013), doi:10.1088/0957-0233/24/3/035301.

[23] A. Kendall and M. Koochesfahani, "A Method for Estimating Wall Friction in Turbulent Wall-bounded Flows," *Exp Fluids*, **44**(5), pp. 773–780 (2007), doi:10.1007/s00348-007-0433-9.

[24] W. M. Kays, M. E. Crawford, and B. Weigand, *Convective Heat and Mass Transfer*, McGraw-Hill (2012).

[25] P. R. Bevington and D. K. Robinson, *Data Reduction and Error Analysis*, McGraw–Hill, New York (2003).

[26] H. W. Coleman and W. G. Steele, *Experimentation, Validation, and Uncertainty Analysis for Engineers*, John Wiley & Sons (2009), doi:10.1002/9780470485682.